FUNDAMENTALS OF ATOMIC AND MOLECULAR SPECTROSCOPY IN INSTRUMENTAL ANALYSIS

S. RAM*

I. INTRODUCTION

The atomic and molecular spectroscopy is a powerful tool to analyse chemical composition or structure of a substance, which may be a pure compound or a simply mixture or solution of two or more different phases of a crystalline or amorphous material. The chemistry and industry people sometimes also talk of minerals, ores, and pollutants, but these comprise the same crystalline or amorphous structures. They are characterized using the same instrumental techniques.

The various techniques explored to characterise these materials using the atomic and molecular spectroscopy constitute a wide subject of basic and applied sciences. Those deal with the interaction of electric or magnetic field or electromagnetic radiation (including the electron beam) with matter through :

(i)   spin or orbital motion of valence electron(s),
(ii) excitation of an electron from a core level of an atom or molecule,
(iii) vibration of nuclie about their equilibrium positions in the molecule, or
(iv) rotation of molecule about the symmetry axes.

The statistical distribution of the interaction probability over the energy scale is called the spectrum and the discipline under which these interactions are studied is called spectroscopy. Thus, according

* Materials Processing Division, National Metallurgical Laboratory, Jamshedpur-831 007.

to the nature or transition-energy of the interaction, the following main branches of spectroscopy have been recognised:

(i)   Vibrational (infrared) or electronic (optical) absorption spectroscopy

(ii)   Vibrational Raman scattering

(iii) Electronic Raman scattering

(iv)   Emission (electronic, vibronic and robronic) spectroscopy

(v)   Electronic fluorescence

(vi)   Phosphorescence

(vii) X-ray scattering

(viii) X-ray photo-electron spectroscopy

(ix)   X-ray fluorescence

(x)   Magnetic resonance (EPR, NMR & FMR)

(xi)   Mössbauer spectroscopy

(xii) Photoacaustic spectroscopy, and

(xiii) Neutron scattering

In neutron scattering spectroscopy, we measure intensity of a neutron beam reflected from different nuclie as well as from electron clouds of associated atoms of given crystal lattice. A neutron bean having no electronic charge, but being a magnetic particle (with magnetic spin $I = 1/2$), easily pentrates the electron cloud and reaches the nucleus. It is therefore more informative than the X-ray or electron scattering to provide accurate positions of different atoms in a crystal lattice. Moreover, it measures also magnetic moments, if any, of individual atoms in the crystal lattice.

In the following discussion, I will confine myself to basically vibrational and electronic spectroscopy using typical examples of :

(i)   inorganic or organic materials

(ii)   glasses and composites, and

(iii) minerals and pollutants.

A basic advantage of these techniques is that they take into account the short range interactions and thus successfully apply to structural diagnosis of crystalline as well as amorphous materials, where X-ray diffraction and most other aforesaid techniques failed. In this sense, the vibrational or electronic spectroscopy is very rewarding to unambiguously determine and confirm the local stuctures, conformers, hydrogen bonding, vibrational or electronic coupling between the structural units, if any, or electron-phonon coupling (including the Jahn-Teller interactions).

II. ELECTRONIC SPECTROSCOPY

A. *Atomic spectroscopy*

Atomic spectrum of an element in solid, liquid or gas phase can be studied by recording or photographing absorption, emission, fluorescence or phosphorescence of the specimen, as defined in Fig-1.
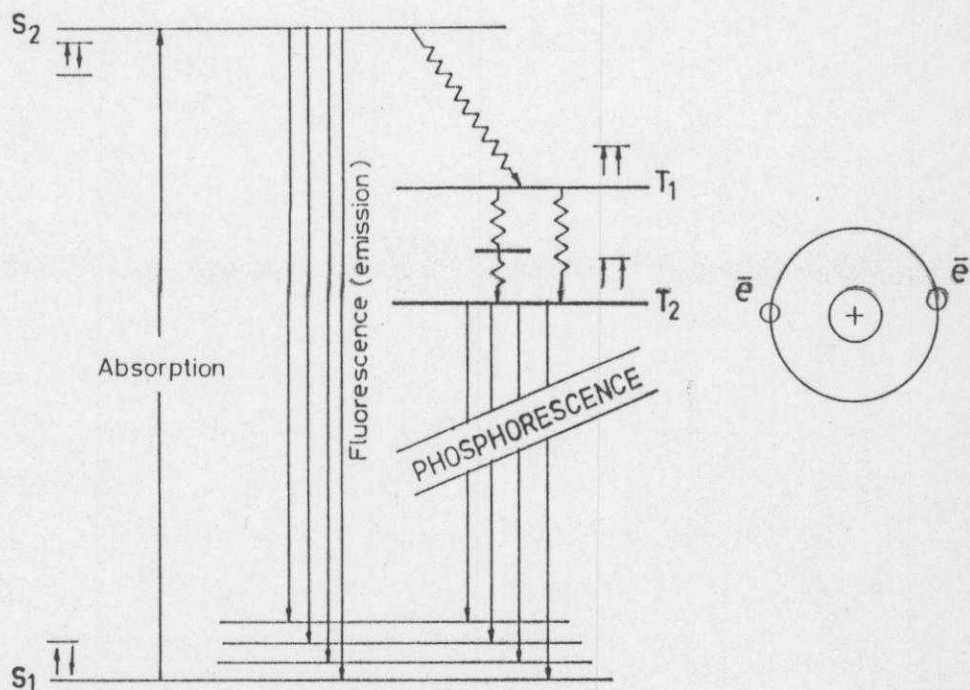

Fig-1 Different competitive processes in electronic excitation of a valence electron.

Atomic absorption of a liquid or gas specimen is monitored by measuring relative intensity of a continuous radiation transmitted through the specimen as a function of wavelength, as shown in Fig.2. The device is set-up and callibrated in a fashion that it measures the absorption or transmission as a function of λ. The spectrum of a solid specimen can be measured in similar way but one has to optimise with the absorption or transmittance of the specimen within the range of the spectrophotometer, i.e. the sample should be appropriately thin of less than ~ 1 mm or it should be diluted by mixing with certain (transparent) additives to allow measurable transmission of the incident radiation through it.
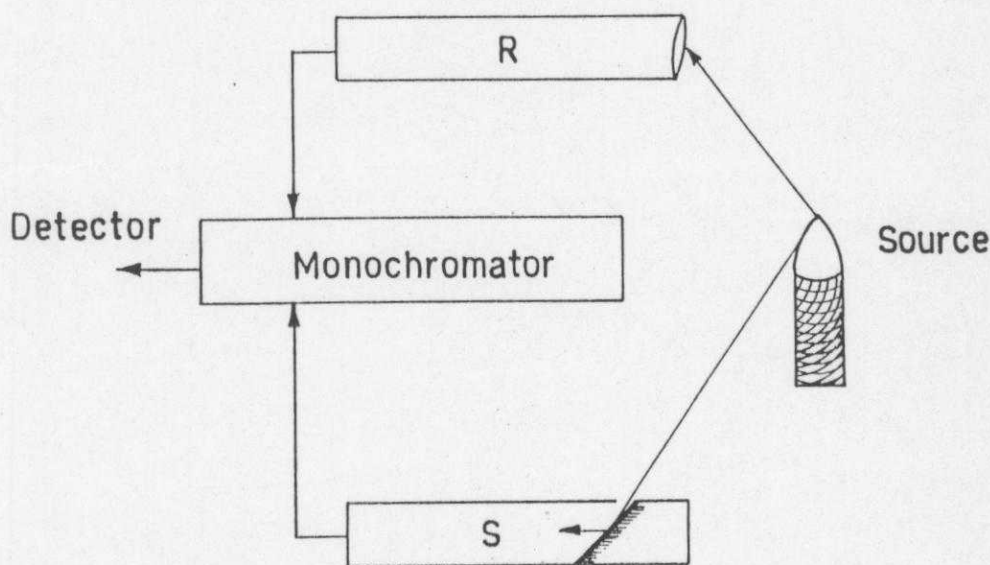

Fig-2 Schematic diagram of measuring absorption spectrum

The emission spectrum is recorded in similar fashion but exciting the specimen in a gap by Arc, spark or discharge. In the fluorescence or phosphorescence, the specimen is excited in a particular electronic state, usually by a laser beam at a given λ, and the spectrum in the transitions from that or lower energy levels to the ground state levels is measured through a monochromater. This technique is usually limited to insulators, i.e. oxides, halides, etc. It can not be applied to metals or other conductors with electrons or holes as the

highly mobile charge carriers. They very rapidly (within 10^{-9}s return from an excited state to the grand state (through electronic conduction and non-radiative transitions) prior to the radiative transition (fluorescence or phosphorescence) is recorded on a monochromator.

B.   Hydrogen atom (IS[1])

Hydrogen is the simplest example to understand the electronic spectrum of an atom or molecule having one or more free (or non-bonding) electron(s). Such a system exhibits stationary states   of energies E_n of the free electrons, following the schrödinger relation

$$H\varphi = E\varphi \qquad (1)$$
where
$$H = (P^2/8\pi^2 m) \Delta^2 + V \qquad (2)$$

is the Hamiltonian. The solution of relation (1) gives
$$E_n = Rz^2 ch/n^2, \qquad (3)$$
$$\text{with} \quad R = 2\pi^2 me^4/[ch^3(4\pi\varepsilon)^2]$$

the Rydberg constant. Other terms have their usual meanings.

Thus a moving electron in a stationary state φ_n radiates an energy

$$\Delta E = E_n - E_m \qquad (4)$$
$$= Rz^2 ch \ (1/n^2 - 1/m^2), \text{ or}$$
$$v = Rz^2 \ (1/n^2 - 1/m^2) \qquad\qquad (v = E/ch) \qquad (5)$$

when it jumps from a state φ_n to another state φ_m. Here, v is wave-number (expressed in cm^{-1}) and n and m are principal quantum numbers.

For hydrogen, with atomic number 1, z=1 and n=1 in the ground IS[1] (^1S_o) electronic state. In excited states φ_m, can assume any

integral values m=2,3,4 .... ∞. Thus for n=1 and m = 2,3,4.... etc., i.e. if an electron jumps from an excited φ_m state to ground state φ_1, in eqn.(4) we get a series of different lines, called Lyman series. Similarly, the $\varphi_m \longrightarrow \varphi_n$ transitions result :

$\varphi_m \longrightarrow \varphi_2$ Balmer series

$\varphi_m \longrightarrow \varphi_3$ Paschen series

$\varphi_m \longrightarrow \varphi_4$ Brackett series, and

$\varphi_m \longrightarrow \varphi_5$ Pfund series,

with m= n+1, n+2 .... etc., respectively. Other details are shown in Fig.3.
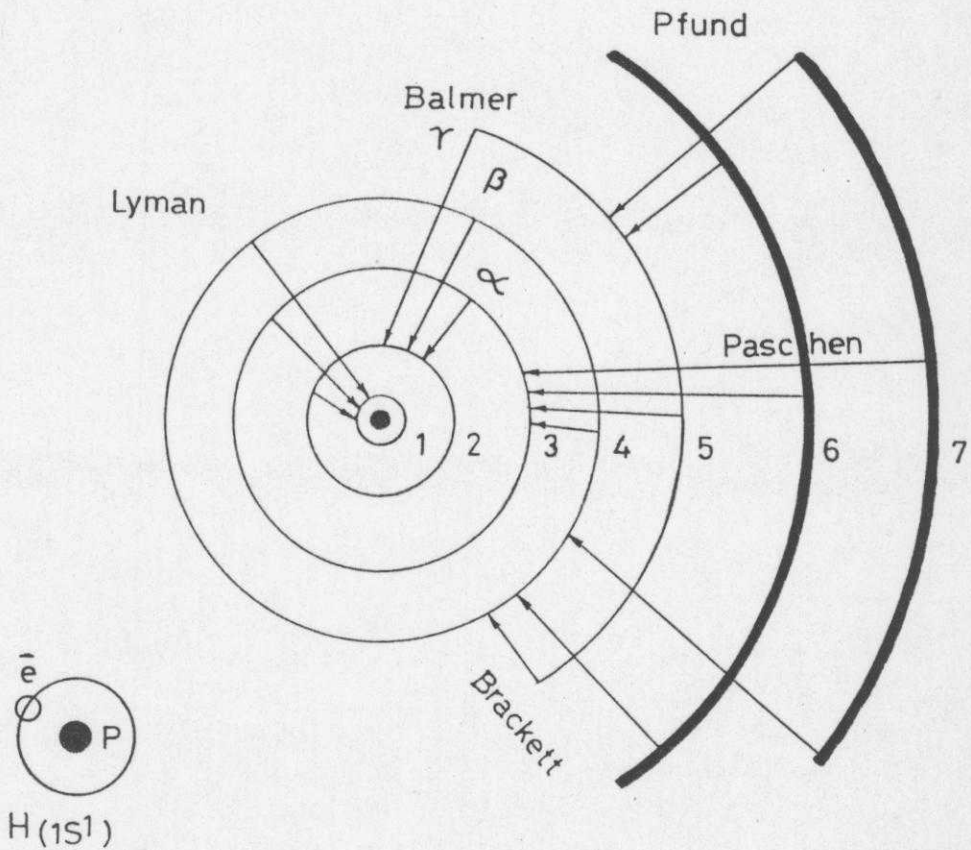
Fig.3 Emission spectrum of hydrogen.

C. *Transition Metals*

(i) Cr^{3+}/Cr^{6+} spectrum

Most of the minerals, in which we might be interested for practical purposes, contain transition metals, rare-earths and actinide series. These having $3d^n$, $4f^m$ & $5f^m$ (with n = 1 → 10 and m = 1 → 14) unfilled subshells of valence electrons exhibit d → d and f f transitions lying in the region extending from far infrared to ultravoilet region of the electromagnetic spectrum. Unlike to hydrogen or alkali and alkaline series, here the electron exclusively does not under go a transition from a given subshell to another subshell but exhibits well-resolved spectrum owing to transitions within the subshell itself. In fact, these transitions are forbidden by the basic selection rules. They become allowed in these particular examples due to pecularly strong spin-lattice interactions, and thus exhibit reasonably intense spectrum,

For example, Fig.4 shows absorption spectra of virgin and heat-treated $50PbO-20Cr_2O_3-30B_2O_3$ glasses. Two characteristically broad bands, marked by arrows at (i) 890 nm and (ii) 694 nm, are observed in the virgin glass (a). Annealing few hours at 500°C or 700°C induces the absorption in the visible and uv regions (starts from 800 nm and grows continuously towards the uv region) at the expense of the absorption in the near IR region. This markes these glass-ceramic products practically useful for opticl glasses/filters or coating materials of different absorption grades for the visible radiation and with almost transparent behaviour for the near infrared radiation. Glasses (b) and (c) provide a sufficiently wide region of practically constant absorption between 740 and 540 nm which was not affected considerably on further heating at temperatures as high as 700°C.
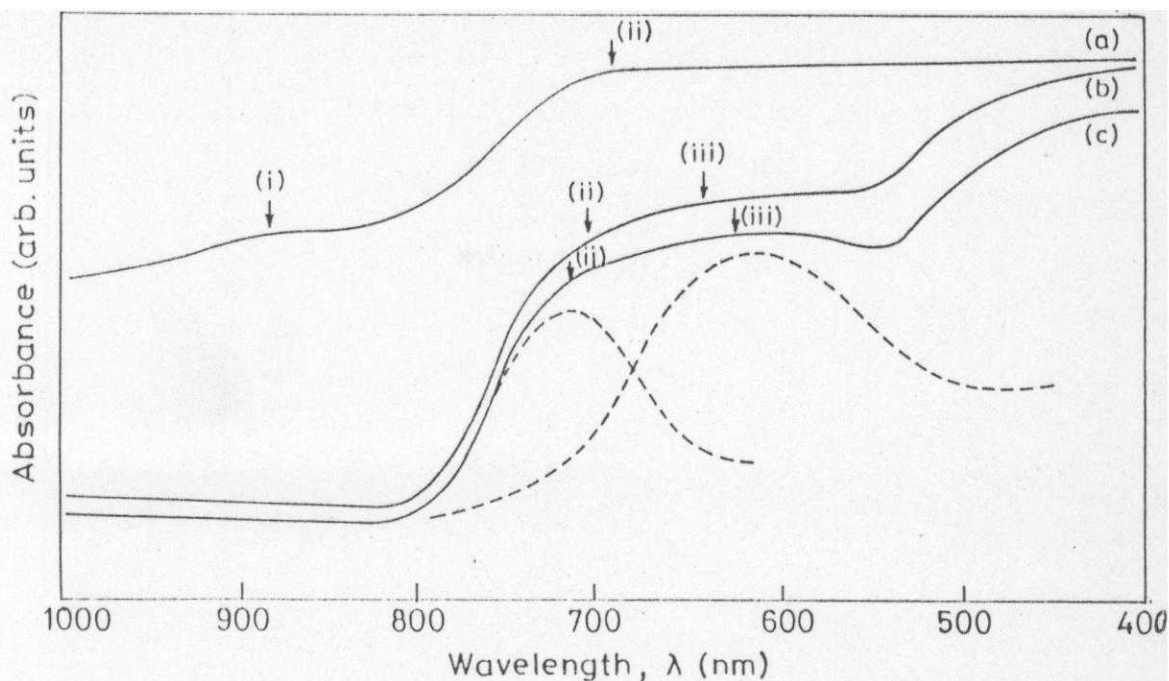
Fig.4 absorption spectra of 50PbO-20Cr$_2$O$_3$-30B$_2$O$_3$ glasses; (a) as-prepared and (b) and (c) recrystallized 2h at 500°C and 700°C respectively. Arrows indicate aver‾avege positions of the absorption maxima analysed using Lorentzian shapes.

The two bands observed at 890 and 690 nm in the virgin glass are assigned to two d-d transitations of Cr^{3+} (3d^3) excited from ground state ^{4}A$_2$ to first excited states ^{4}T$_2$ and ^{2}E, ^{2}T$_2$, respectively. Here, the ^{4}A$_2 \longrightarrow {}^2$E, ^{2}T$_2$ transitions are spin-forbidden but they surprisingly exhibit ambiguously much stronger intensity than in the spin-allowed ^{4}A$_2 \longrightarrow {}^4$T$_2$ transition[1].

It is likely that the chromium in the present glasses exists in a thermodynamic Cr$^{3+} \rightleftharpoons$ Cr^{6+} equilibrium, with Cr^{3+} and Cr^{6+} oxidation states. The presence of chromium in the different oxidation states allows their intermixing, through the spin-couping, to reveal modified energy levels of the coupled "Cr^{3+}-Cr^{6+}" ion-pairs. The energy levels of the ground and excited states of isolated Cr^{3+} and Cr^{6+} are portrayed in Fig-5. The transition between ground state ^{4}A$_2$ and the excited state ^{2}E or ^{2}T$_1$ of Cr^{3+} or that between ground state ^{1}A$_1$ and the first excited state ^{3}A$_2$ of Cr^{6+} is forbidden by both symmetry

as well as spin. As the electrons of Cr^{3+} couple with those of Cr^{6+}, the transition between the excited and ground states becomes spin allowed, as shown in Fig-5 for the "Cr^{3+}— Cr^{6+}" compled pair, accounting for the large intensity of the 694 nm bandgroup observed in the present samples.
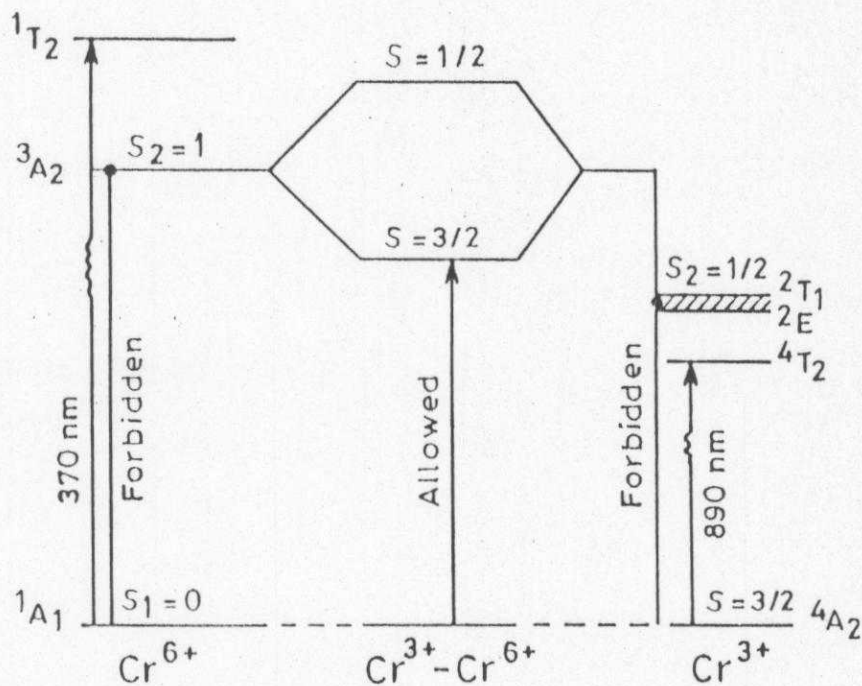

Fig.5 Schematic diagram for spin coupling between the ground and $^3A_2$ and ^2E, $^2T_1$ excited states of isolated Cr^{6+} and Cr^{3+}. The shaded area indicates the overlapping region between ^2E and $^2T_1$ excited states of Cr^{3+}.

Formation of similar coupled "ion-pairs" in Mn^{2+} doped $RbMgF_3$ crystals[2] led to the intensity of a spin forbbiden $^6A_1 \rightarrow {}^4T_1$ transition of Mn^{2+} enhanced by a factor of 10^5. In these crystals, the Mn^{2+} occupy two crystallographically different Mg^{2+} sites, and therefore exhibit two distinctly different emission and excitation spectra. The energies of the absorption and emission bands associated with these sites are summarized in Table-I. These spectra are reproduced in Fig.6.

Fig.6 (a) shows a 710 nm emission band (dashed line) and its excitation spectrum (solid line) with peaks at 420 and 600 nm. Fig 6(b) shows an 870 nm emission band and its excitation spectrum with peaks at 430 and 700 nm. Lifetimes (τ) measured for both transitions are found to be $\tau \sim 20$ ms. This is consistent with an oscillator strength of $f \sim 10^{-3}$ determined using the relation :

$$f = 4.32 \times 10^{-9} \int \epsilon \, dv \qquad (6)$$

—— where the integral defines the area under the absorption curve.

Table-I. Absorption and emission bands of Mn^{2+}: $RbMgF_3$ crystals

	Irradiated		Irradiated & annealed
	Site-I	Site-II	(in nm)
	(in nm)		
Absorption :			
$^6A_1 \rightarrow {}^4E, {}^4A_1$	420	430	410
$^6A_1 \rightarrow {}^4T_1$	600	700	700
Emission :			
$^4T_1 \rightarrow {}^6A_1$	710	870	870

   A required condition for mixing of the free-ion wavefunctions with those of the neighbour ions or the lattice vibrations is that the symmetry associated with the centre of inversion be destroyed by the neighbours. This is evident from our vibrational analysis of the various glasses, shown in Table-II, where the degeneracies of $v_2(E)$ and v_3, $v_4(F_2)$ vibrational modes of CrO_4^{2-} are completely removed, confirming a site symmetry for CrO_4^{2-} lower than a T_d symmetry[3]. This can be accomplished both dynamically (via odd parity vibrations) and statistically (as a result of the odd-parity distortions present in the

system). A small 1-5 mol% addition of Al_2O_3 (acts as a glass network modifier) in these glasses causes non-bridging oxygens and produces heterogenous nucleation centres in the glass, reducing locally ordered structure of CrO_4^{2-} (and also borate) groups. It is clearly reflected in significantly enhanced bandwith as well as the intensity of absorption maximum at ~ 700 nm. This provides a good example of dynamically induced intensity mechanism.
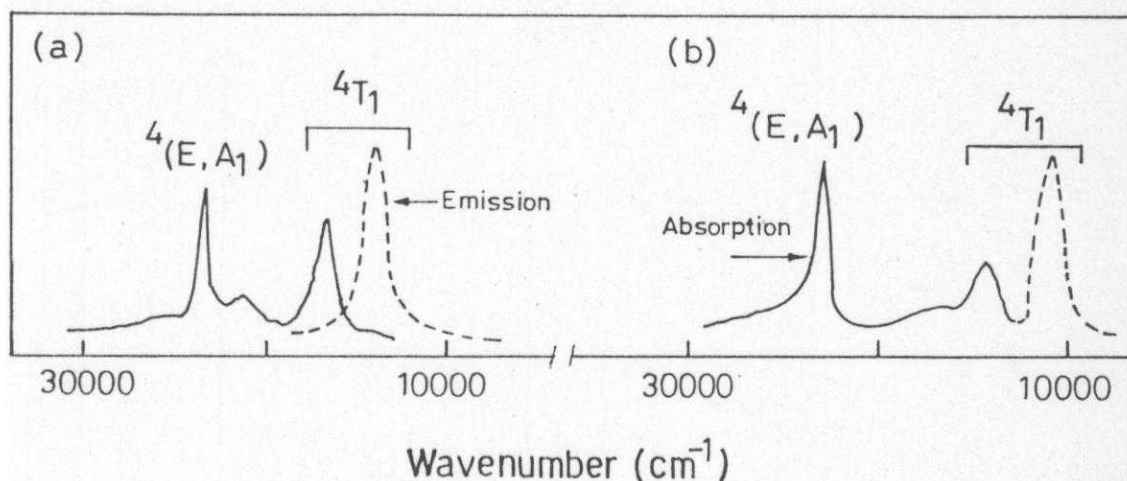

Fig.6. (a) 710 nm emission band (dashed line) of Mn^{2+}: $RbMgF_3$. Its excitation spectrum is shown by the solid line. (b) shows excitation spectrum of an 870 nm emission band.

Crystalline $PbCrO_4$ or Pb_2CrO_5 developed in the heat-treated glasses exhibit charge transfer bands of CrO_4^{2-} chromophore, but they lie far below in the uv region[4]. Moreover, Toda and Morita[5-7] reported that Pb_2CrO_5 shows photoconduction with an optical bandgap-energy E_p ~ 2.1 eV (or 570 nm). Indeed a strong absorption band group occurs around 600 nm, especially in Al_2O_3 added glasses, due to an electronic excitation through this optical bandgap. The position of this

Table-II. IR and Raman bands (cm^{-1}) observed in Pb_2CrO_5 microcrystals precipitated in $PbOCr_2O_3$-B_2O_3 glasses*

IR	Raman	CrO^{2-} bands in H_2O solution**	Assessment
325 (vw)	330(w)	348	$v_2(E)$
375 (ms)	373 ms)	368	$v_4(F_2)$
-	380 (w)		
865 (vs)	860 (vs)	847	$v_1(A_1)$
890 (s)	890 (w)***		
	905 (ms)	884	$v_3(F_2)$
935 (sh)***	933(vs)		

*   Samples are bleached in weak hydrochloric acid.
** Raman bands observed in aqueous K_2CrO_4 solution.
*** Bands are too weak and could be observed only at low (liquid N_2) temperatures. Relative intensities are given in the parentheses : w = weak, uw = very weak, s = strong, ms = medium strong, vs = very strong, sh = shoulder.

bandgroup is very sensitive to the impurities incorporated in these crystals during their crystallization from these glasses. A glass specimen achieved a significantly large 80% crystallized volume fraction of Pb_2CrO_5 as the only crystallise phase thus exhibited an absorption maximum at 578 nm, fairly consistent with the optical bandgap determined by the photoconduction measurements on Pb_2CrO_5 single crystals.

(ii) *Fe²⁺ (3d⁶) spectrum*

The d^6 - electron spectrum of Fe^{2+} ion in metals or metal salts has been extensively studied[8]. The ground state ^5D (L = 2 and S = 2) of the free Fe^{2+} ion in T_d symmetry is split into an orbital doublet ^5E and a triplet $^5T_2$ (separated by $\Delta = 10/D_q$) by the crystal field. Furthermore, the spin - orbit interaction removes degeneracy of the ground state ^5E, which is ultimately spilt into five different nearly equally spaced levels (Γ_1 , Γ_4 , Γ_3 , Γ_5 and Γ_2) separated by $6\lambda^2/\Delta$, with $\lambda = -100$ cm⁻¹ the spin-orbit interaction parameter, as shown in Fig.7.
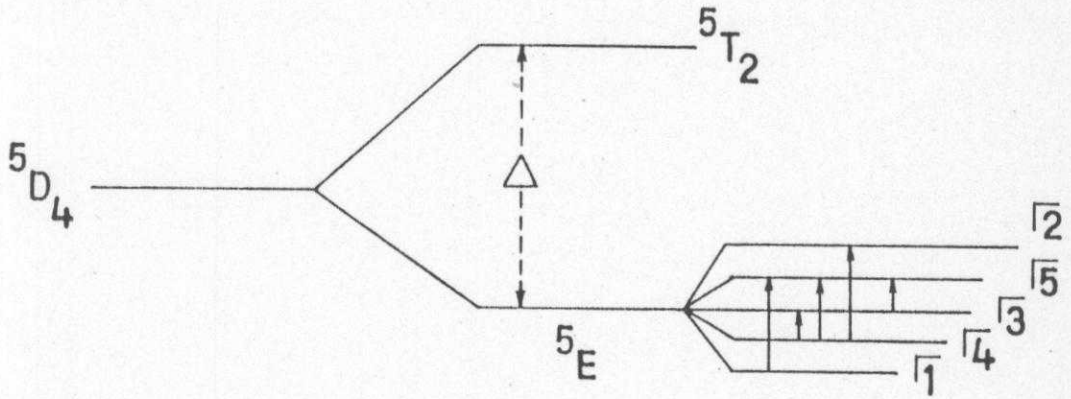
Fig-7 Crystal field splitting of Fe^{2+} free ion in T_d symmetry

Optical transitions from the singlet Γ_1 ground state to levels of $^5T_2$ have been seen near 2500cm⁻¹. The transitions among the ^5E split levels (allowed by electric dipole are marked by the arrows in Fig.7) appear in far IR region. For example, Fig.8 shows a typical spectrum of Fe^{2+} : $Cd_{0.99} Fe_{0.01}Te$. The lowest energy line in $\Gamma_1 \rightarrow \Gamma_4$ transition occurs at 18.6 cm⁻¹. Electronic transitions inside the ^5E multiplet are strong function of the interaction (Jahn-Teller effect) between the $d^6(Fe^{2+})$ electrons and the lattice vibrations.
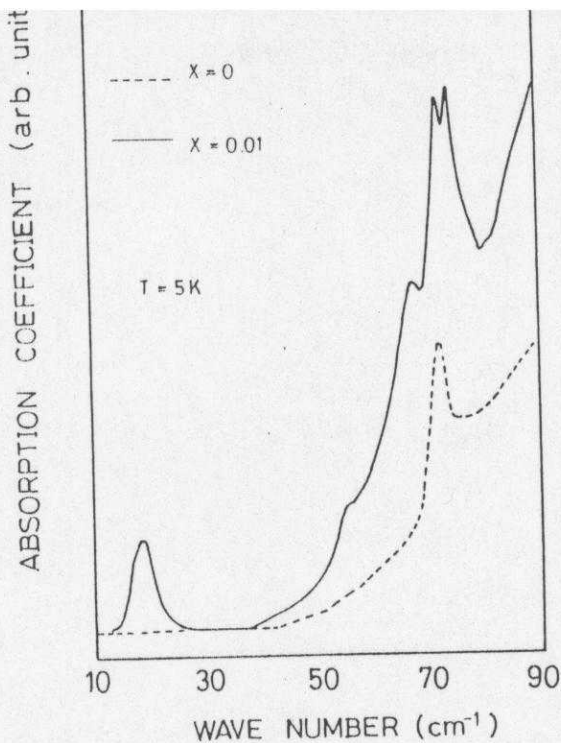
Fig.8. Far IR spectra of $Cd_{1-x}Fe_xTe$ (x = o and 0.01 at 5K.

(iii) Fe^{3+} $(3d^5)$ spectrum

The ground state of iron in Fe^{3+} state is $^6A_1(S)$. It exhibits the first absorption band at around 690 nm in the transition to the first excited state $^4T_1(G)$. Obviously, the Fe^{3+} is transparent to IR and near IR radiations but strongly absorbs in visible region and very strongly in the uv region with cut-off energy at about 350 nm. Thus it is very easy to anambiguously distinguish from Fe^{2+} centres.

$^4T_1(G)$ excited state of Fe^{3+} has a reasonably long lifetime of 25.2 ms. It therefore exhibits very intense fluorescence to the ground state and associated vibronic states. The possible transitions of Fe^{3+} are therefore well-resolved in Fe^{3+} doped crystals such as ZnO (which does not have its own absorption in this region[9]). These allowed accurate analysis of the fine structure of $T_1(G)$ state and in-turn site symmetry of Fe^{3+} in the associated crystals.

(iv) Cu^{2+} $(3d^9)$ spectrum

I think there is no need to point out unlimited applications of copper and copper materials in industry, technology as well as in basic research. We have been using the copper in one or the other way since the copper age. Their optical spectroscopy, with characteristically sharp and well-resolved d-d electronic transitions, is very sensitive to unambiguously detect them in the minerals and salts even if they are present at trace levels.

Of the 3d transition metals, Cu^{+2} $(3d^9)$ has one of the most simple electron systems and is most amenable to testing posulates of crystal field theory and the Jahn-Teller effect. It exhibits very low lying energy levels in the infrared region. Those are useful to control and vary the optical and electrical properties of the Cu^{+2} doped ZnO[10], ZnS[11], CdS[12], $CdTe$[13] or $ZnTe$[14] semiconductors. The Cu^{+2} doped lasers, sensors and optical storage materials of the present decade are the best cmpliments of these d-d electron transitions.

Figure 9 shows a typical absorption spectrum of Cu^{2+}: ZnTe, as recently reported by Volz et al[14]. The most intense peak at $v_o = 1069$ cm^{-1} is attributed to a zero-phonon transition from spin-orbit split ground state $^2T_2$ (Γ_7) to the first excited state ^2E (Γ_8), schematically portrayed in Fig.10. The set of absorption lines A begining at $1069 cm^{-1}$ and ending at approximately 1200 cm^{-1} is repeated in sets B and C by a constant energy interval of 210 cm^{-1}. This energy interval corresponds to the v_o mode of the lattice vibration and compares well with a value of 207 cm^{-1} obtained from neutron scattering data[15].

The integrated (total area) intensities of the first peaks of each set follow a Poisson distribution, expected for electron-phonon coupling. The strength of the electron (LO)-phonon coupling measured here is given by a Huang-Rhys factor $S=0.8$. However, the absorption peaks under each set do not so satisfactorily follow the Poission distribution of their intensities.
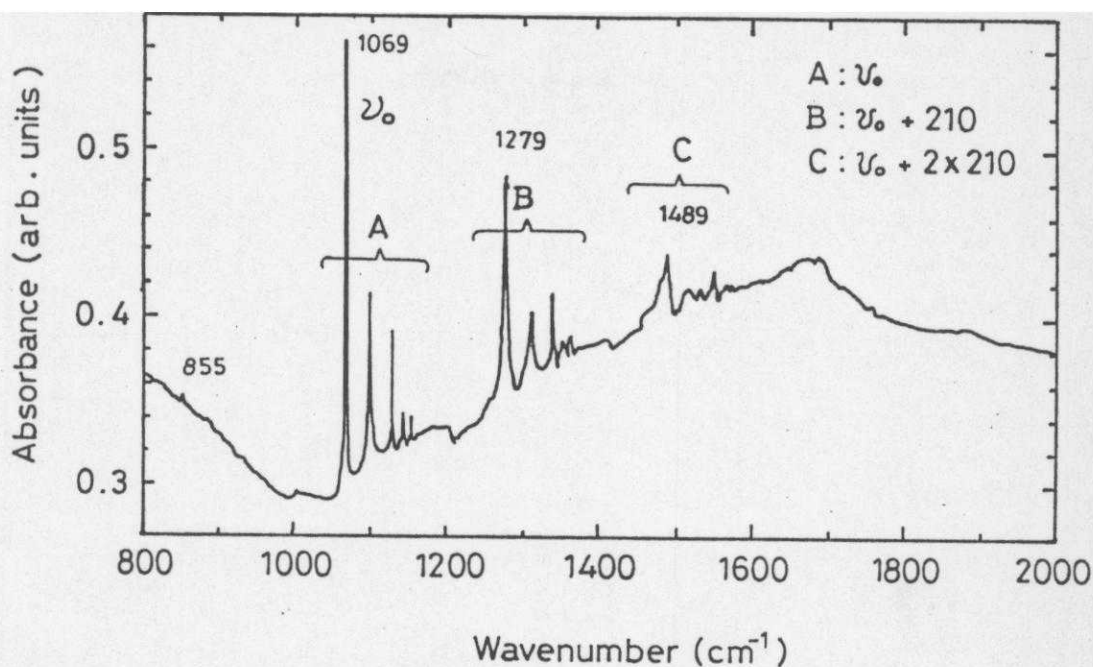
Fig. 9. Infrared spectrum of Cu^{2+}:ZnTe at 4.6 K.

Another set of absorption lines has been observed between 850 and 950 cm^{-1}. It has same internal spacing as does the set of lines A between 1050 and 1200 cm^{-1}. These lines are attributed to the anti-Stokes portion of the spectrum. Two zero-phonon lines are also identified. In addition to the prominent zero-phonon line at 1069 cm^{-1}, a second zero-phonon line of considerably much lower intensity is confirmed at 1002 cm^{-1}. This zero-phonon line is assigned to the transition $^2T_2$ (Γ_8) $\rightarrow$ ^2E (Γ_8). A complete diagram of these two transitions is summarized in Fig.10.

The absorption spectrum measured on a rather high resolution between 1050 and 1200cm^{-1} is shown in Fig.11. It comprises six different irregularly spaced phonon modes. The third one lies only 4 cm^{-1} away from the second. The bands observed in this region are not in a sequence of constant-energy differences and do not exactly
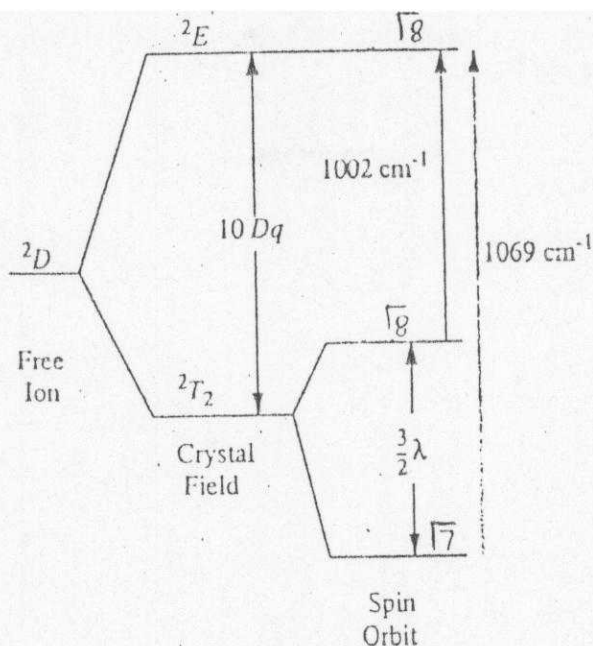
Fig.10 Energy-level diagram of the ^2D term split by a crystal field of T_d symmetry and spin-orbit coupling.

match with the lattice phonons. For example, the energy difference between the zero-phonon line at 1069 cm^{-1} and the first succeeding absorption line within the set is 32 cm^{-1}, considerably less than the value of a nearest phonon mode of 42 cm^{-1}, determined by the neutron scattering. This irregular nature of these phonon lines can be understood by invoking the contribution of dynamic Jahn-Teller effect on these phonons.

D. **Rare-earth cations**

In this example, I discuss some peculiar features of rare-earth compounds. The rare-earth(R) elements, which of course are not rare in our country (we are the third largest producer of rare-earth minerals in the world), have unfilled 4f subshells of electronic configuration

$$R : 4f^n(5S^25P^6)6S^2 \qquad (7)$$
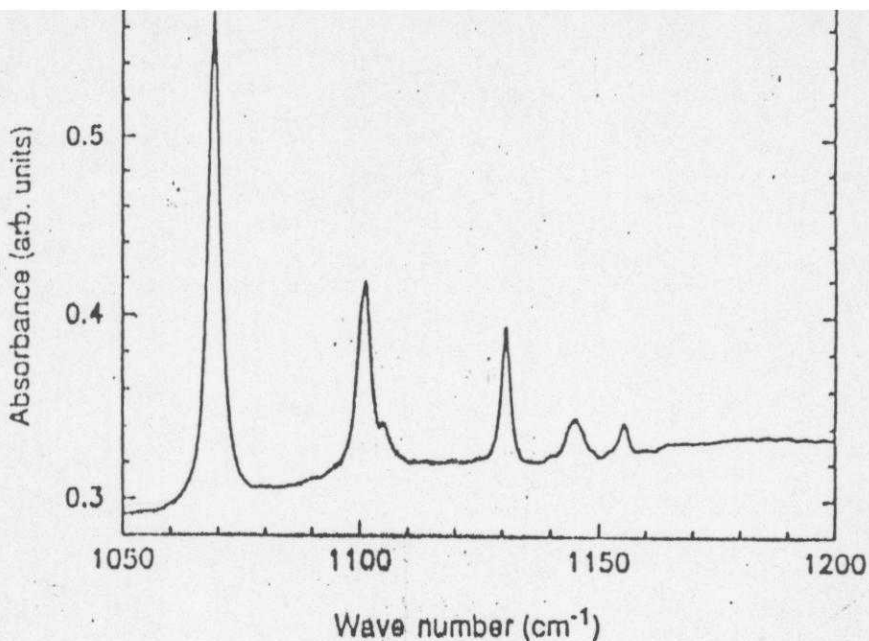
Fig.11. High resolution IR absorption spectrum of Cu^{2+}: ZnTe (after Volz et.al 1992)

with $n = 1 \rightarrow 14$. They usually (except cerium which exists as Ce^{4+} and Ce^{2+}) exist in R^{3+} oxidation state having the electronic configuration

$$R^{3+}: 4f^{n-1} (5S^2 5P^6) \qquad (8)$$

i.e. the $4f^{n-1}$ electrons are shielded by $5S^2 5P^6$ electrons and this is the reason that the rare-earth salts (unlike the transition metal salts) usually exhibit characteristically sharp and well-resolved electronic transitions in absorption as well as in the emission spectrum. Also the actinide series exhibits similar valence electrons ($5f^n$) and similarly sharp 5f - 5f transitions.

(i) **Eu³⁺ (4f⁶) spectrum**

Fig.12 shows absorption spetrum of Eu^{3+} of a N, N- dimethyl-diphenyl-phosphinamide (DDPA) adduct of europium   perrhenate, which is written as $Eu(ReO_4)_3$. 2DDPA.   Some vibronic bands associated with the eletronic transitions are accompanied by blue shifted broad bands. These are makred by the plus (+) sign. The band

positions and oscillator strengths of the principal bandgroups assigned for a few low-lying energy transitions are given in Table-III.
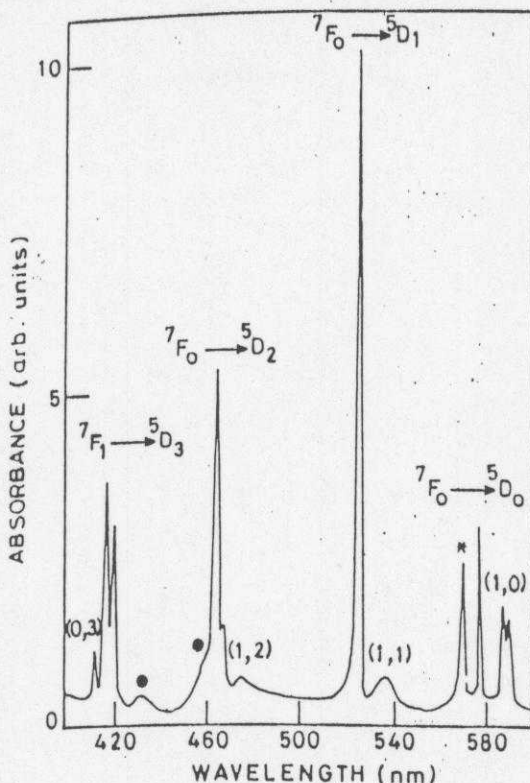
Fig.12 Absorption spectrum (600–400 nm) of the Eu(III) ion in $Eu(ReO_4)_3 \cdot 2DDPA$ at 300 K. (*) Absorption of Re^{4+}, ($\oplus$) vibronic bands.

The oscillator strengths of the bands have been calculated using the integral area under the absorption curves (for details see Feuerhelm et. al.[16]). Their values so obtained for the $^7F_0 \rightarrow {}^5D_J$ (J = 0– 4) bands are of particular interest in elucidating the electric/magnetic dipole characters and hence the $4f \rightarrow 4f$ radiative transition probabilities. Amongest these transitions, only $^7Fo - {}^5D_1$ satisfies the magnetic dipole selection rules $\Delta J = 0, \pm 1$, with J = $0 \nleftrightarrow 0$) in an intermediate coupling scheme[17]. The $^7F_0 \rightarrow {}^5D_{2, 4}$ transitions are believed to be primarily electric dipole in character. Their intensities are therefore strongly dependent on crystal field effects. The $^7F_0 - {}^5D_3$ transition has a mixed character, while the remaining $^7F_0 - {}^5D_0$ transition is regorously forbidden for any magnetic/electric dipole or electric quadrupole transition. This transition usually appear in non-centrosymmetric europium compounds.

Table-III. Principal absorption bands of Eu(III) In $Eu(ReO_4)_3 \cdot 2DDPA$ observed at 300 K

Wavelength (nm)	Oscillator strength ($f \times 10^8$)	Transitions
590.0(16,950)	0.023	$^7F_1-{}^5D_0$
588.0(17,007)		
578.4(17,.289)	0.010	$^7F_0-{}^5D_0$
570.0(17,544)	0.013	Re^{4+} band
536.0(18,656)	1.014	$^7F_1-{}^5D_1$
525.0(19,048)	0.50	$^7F_0-{}^5D_1$
472.0(21,186)	0.010	$^7F_1-{}^5D_2$
465.0(21,505)	0.35	$^7F_0-{}^5D_2$
464.0(21,552)		
459.0(21,786)	-	vibronic bands
432.0(23,148)		
420.0(23,895)	0.34	$^7F_1-{}^5D_3$
416.0(24,038)		
412.0(24,272)	0.005	$^7F_0-{}^5D_3$
393.0(25,445)	35	$^7F_0-{}^5L_6$
384.0(26,042)	4.5	$^7F_0-{}^5L_7$
381.0(26,247)	2.5	$^7F_0-{}^5G_{2.3.4}$
377.0(26,525)		
365.0(27,397)	5.0	$^7F_0-{}^5D_4$

Transition energies in cm^{-1} are given in the parentheses.

Thermally excited $^7F_1$ $^5D_3$ bandgroup at 420 nm exhibits ~70 times larger intensity than in the $^7F_0$ $^5D_3$ band excited from the ground state $^7F_0$ at 300 K. The intensity in the former band increases exponentially and decreases in the latter following the Boltzmann population distribution

$$N = N_0 \exp{(-\Delta E/KT)}, \qquad\qquad (9)$$

with increasing temperature between 77 and 650K, confirming their present assignments. Thermally excited bands to $^5D_{0-2}$ levels have also been noted (cf. Table-III) but those are not so pronounced[18].

2J+1 - fold degeneracies of $^5D_1$ and $^5D_2$ states are completely lifted-up in the present compound as evident by the high resolution spectra shown in Fig-13. It means the Eu^{3+} in this compound bears a sufficiently low site symmetry of C_{2v}, C_2, C_s or C_1.
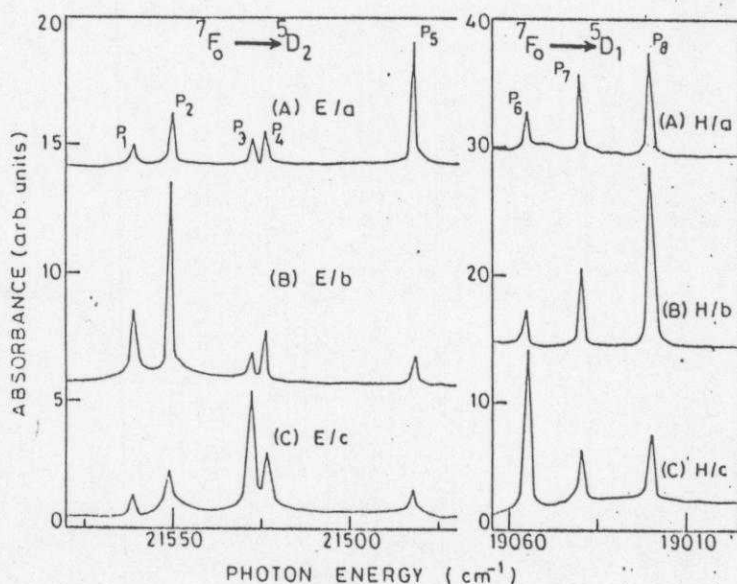
Fig.13 Polarized absorption spectra of the $^7F_0 \rightarrow ^5D_i$ and $^7F_0 \rightarrow ^5D_2$ bands of the Eu(III) ion at ~77 K. The electric vector E for the $^7F_0 \rightarrow ^5D_2$ transition and the magnetic vector H for the $^7F_0 \rightarrow ^5D_1$ transition were kept parallel to a, b, and c crystal axes in (A), (B), and (C), respectively.

It is interesting to note that intensity of absorption from ground state $^7F_0$ to first excited state $^5D_0$ is very poor or zero but the most intense fluorescence always occured from this ($^5D_0$) state to various ^7F_J (J = 0-6) levels as shown in Figs.14 and 15. Hence one should be very careful in analysing concentration of Eu^{3+} cations in unknown samples using these intensities.
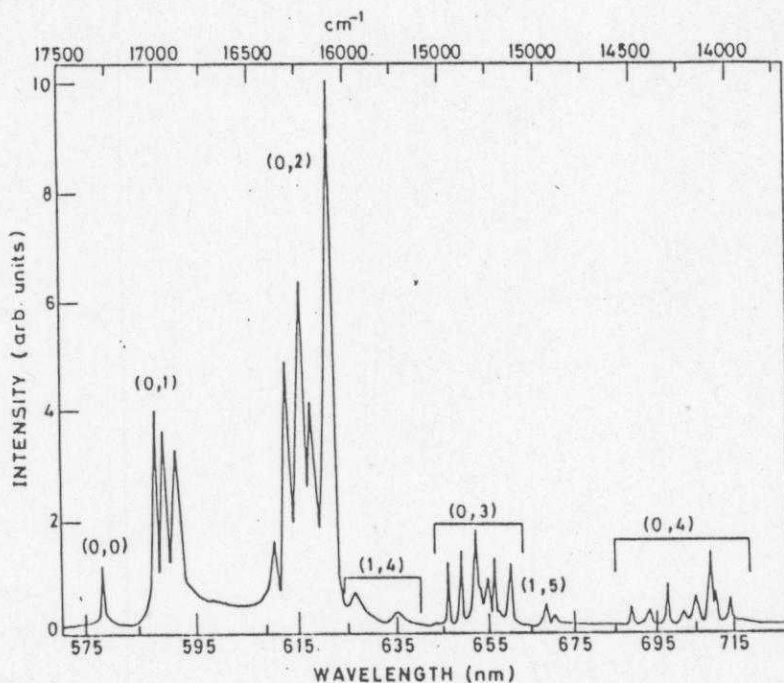

Fig.14 Fluorescence spectrum of the Eu(III) ion in $Eu(ReO_4)_3 \cdot 2DDPA$ at 77 K with the emitting state $^5D_0$. λ_{exc} = 488.0 nm Ar^+ laser.
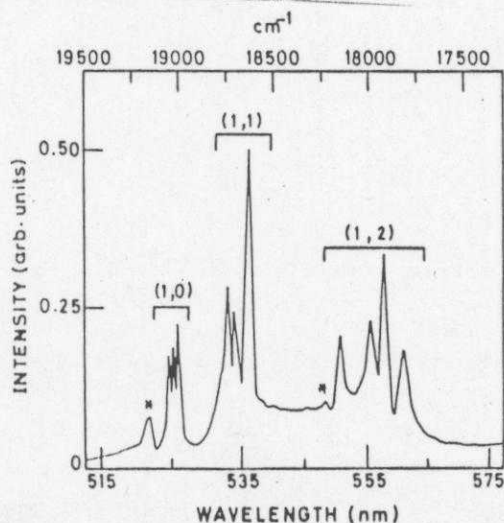
Fig.15 Fluorescence spectrum of the Eu(III) ion corresponding to that of Fig.13 with the principal emitting state $^5D_1$. * = Vibronic bands.

Figure 16 summaries crystal-field levels splitant of ^7F_J multiplets deduced in the fluorescence from ^5D_J (J=0,1,2 & 3) excited states. Intensity distribution over them did not significantly differ in the different excitations. The fluorescence from ^5D_J (J=0−3) levels exhibited optimum intensities for the excitations made with 545.5, 488.0, 465.8 and 457.9 nm Ar$^+$ laser lines respectively. None of the ^5D_J crystal field levels matches completely with any of these laser lines and the fluorescence in each case was induced through excitation of associated vibronic levels. The $^5D_0$ remains the prominent fluorescence state with all the excitations.
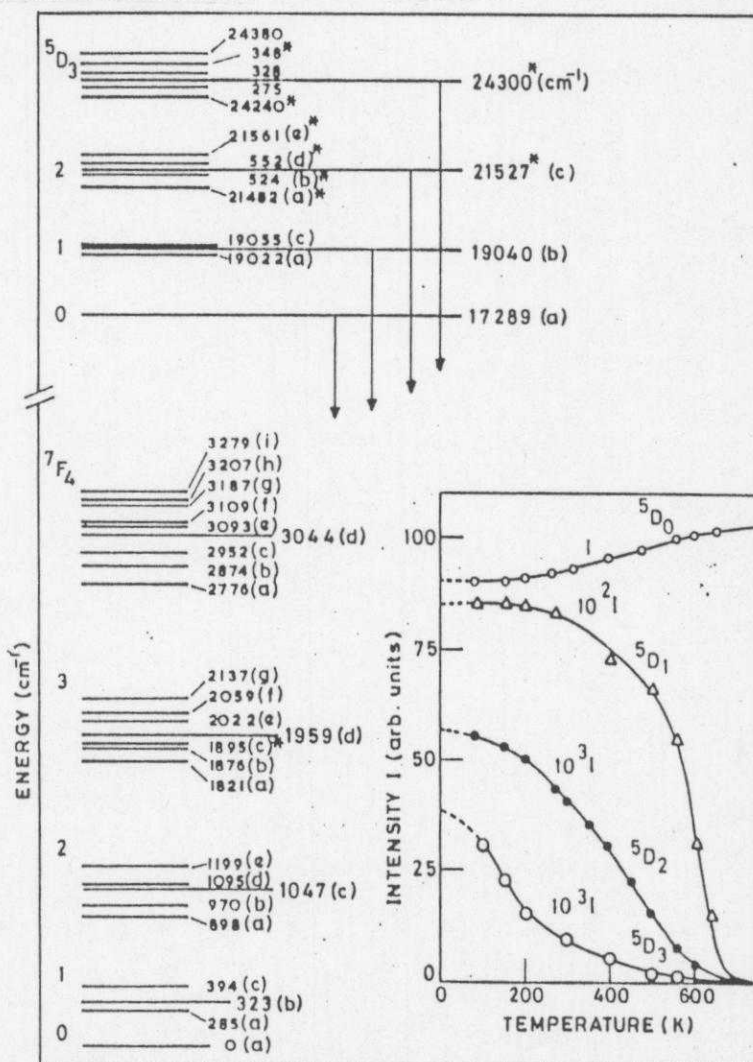
Fig. 16 Stark energy levels (not to scale) of the Eu(III) ion in Eu(ReO$_4$)$_3$ · 2DDPA at 77 K. (*) Data taken from absorption spectrum. The inset figure is the temperature variation of ^5D_J (J = 0 → 3) fluorescence intensity. The intensity scale on the vertical axis is given for $^5D_0$ fluorescence. This is to be multiplied by 10^{-2} and 10^{-3}, respectively, for the $^5D_1$ and $^5D_{2,3}$ fluorescence intensities.

A plot of the fluorescence intensity from various ^5D_J states as a function of temperature is given in the inset Fig-16. The fluorescence originating from $^5D_3$, $^5D_2$ and $^5D_1$ levels show large decrease of intensity with increasing temperature. The rates at which the intensities decrease fall in the order $^5D_3 > {}^5D_2 > {}^5D_1$. On the other hand, the intensity from $^5D_0$ state regularly increases with increasing temerature. Obviously, the higher $^5D_{J>1}$ levels release the associated energies by a combination of radiative (to ^7F_J multiplet) and non-radiative (to $^5D_0$) transitions. The non-radiative transition responsible for thermal quenching of $^5D_{J>1}$ states increases with increasing temperature and leads to population of $^5D_0$ level, and results in the enhanced $^5D_0$—^7F_J fluorescence.

The mechanism of fluorescence from a particular level is a strong function of vibronic coupling. The vibronic coupling governs radiative and nonradiative processes, as summerized in Fig.17 for $Eu_2(SO_4)_3$. $8H_2O$. Addition of a few drops of KI in aqeuous solution of $Eu_2(SO_4)_3$. $8H_2O$ quenches the fluorescence and manifested the electronic Raman transitions through the low lying ^7F_J electronic-energy levels. The H_2O molecules in the aqueous solution are strongly hydrogen bonded. The hydrogen bonding (inter as well as intramolecular) is considerably reduced on the addition of KI due to the formation of

$$K^+ - I \cdots H - O \qquad H$$
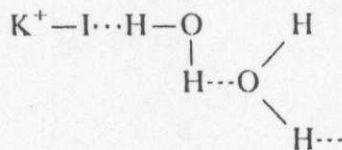
bonds[19]. The effect has been directly reflected in ~ 3% increased O-H strectching frequencies in the range 3130 - 3640cm^{-1}.

(ii) Nd^{3+} (4f^3) Lasers

Neodymium is one of the most demanded rare-earth (R) element, especially after the discovery of the high T_c superconductors and high-energy-density $R_2Fe_{14}B$ or $R_2T_{17}N$ (where T is a transition metal) magnets during the present decade. Nd^{3+} : YAG lasers and
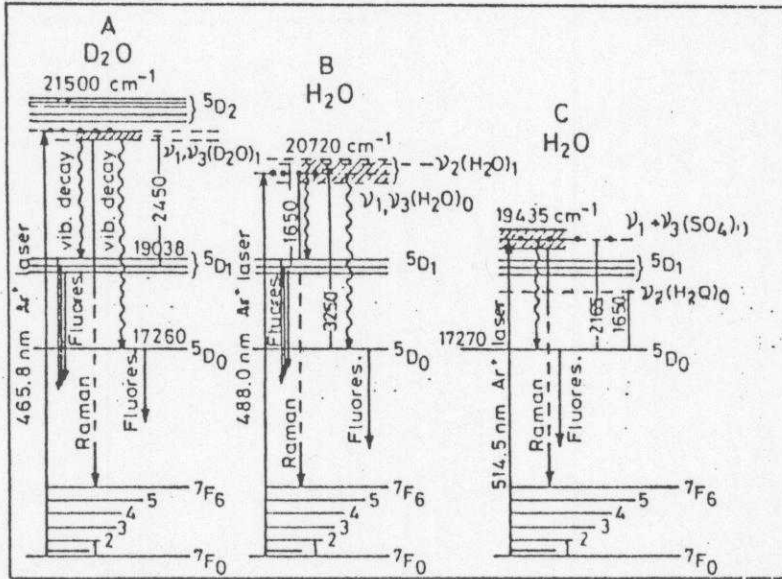

Fig. 17 Schematic energy level diagrams (not to scale) showing the Eu^{3+} fluorescence emission, electronic Raman scattering and several non-radiative processes operative simultaneously in the Eu$_2$(SO$_4$)$_3$ solutions. The emitting states $^5D_1$ or $^5D_0$ are excited through the associated vibronic levels, showing a prominent fluorescence in (A) D$_2$O for λ_{exc}=465.8 nm and (B) H$_2$O for λ_{exc}= 488.0 nm. (C) The fluorescence only from the $^5D_0$ is excited with λ_{exc}=514.5 nm. The vibronic levels are shown by the broken lines. A subscript 0 or 1 outside the parentheses, e.g. ν_i(H$_2$O)$_0$ or ν_i(H$_2$C)$_1$, refers to the J value of the associated ^5D_J electronic level. The shaded region shows the spread of the vibronic levels.

$R_3Fe_5O_{12}$ (RIG) garnets stem other thrust areas of advanced technology of optical, magnetic and electronic devices. We are very fortunate to have a plenty (about 0.4 M tonnes) of neodymium reserves in our country. Table-IV compares world-wise reserves of neodymium. Thus we are among the three richest countries of neodymium resources. However, we are far away from competing the aforesaid technologies.

Table - IV

Estimated reserves of neodymium in different countries

Country	Reserves (in tonnes)
China	4,600,000
U S A	640,000
India	400,000
U S S R	64,000
South Arfica	13,000
Brazil	4,000
Malaysia	4,000
Others	58,000

Figure 18 shows optical absorption spectra of singly or codoped $30BaF_2$-$18InF_3$-$12GaF_3$-$20ZnF_2$-$(10-x-y)YF_3$-$6ThF_4$-$4ZrF_4$-$xCrF_3$- $yNdF_3$ (BlGaZYTZr) fluoride glasses with Cr^{3+} and Nd^{3+}. The spectrum of Cr^{3+} (0.2% singly doped glass (a) is characterized by two spin-allowed broad bands, which can be identified as the vibronically broadened transitions $^4A_2$ — $^4T_2$ at ~ 655 nm and $^4A_2$ — $^4T_1$ at ~ 450 nm. The former band contains a fine structure due to the spin-forbidden $^4A_2$ — ^2E, $^2T_1$ transitions. This glass exhibits a broad structureless fluorescence band centred at ~ 890 nm in $^4T_2$ — $^4A_2$ transition. This fluorescence band exhibits a large Stokes shift ~ 4000cm^{-1} and that strongly decreases with increasing temperature.

The decay kinetics of the broad fluorescence of Cr^{3+} in the fluoride glass were studied as a function temperature and emission wavelength. The decay of the intensity measured along the fluorescence

band using $\lambda_{exc} \sim 655$ nm, i.e. exactly the centre of the $^4A_2 - ^4T_2$ absorption, can be described by a double exponential function throughout the studied temperature range 320-70K. This behaviour persists even for lower Cr^{3+} concentrations upto 0.05%, demonstrating that $Cr^{3+} - Cr^{3+}$ interactions are not very important here. The intensity basically depends on the lifetime and population of the fluorescent species in the fluorescent state. Both these parameters exponentially decrease with increasing temperature in this range and thus account for the observed variation of the fluorescence intensity with the temperature.
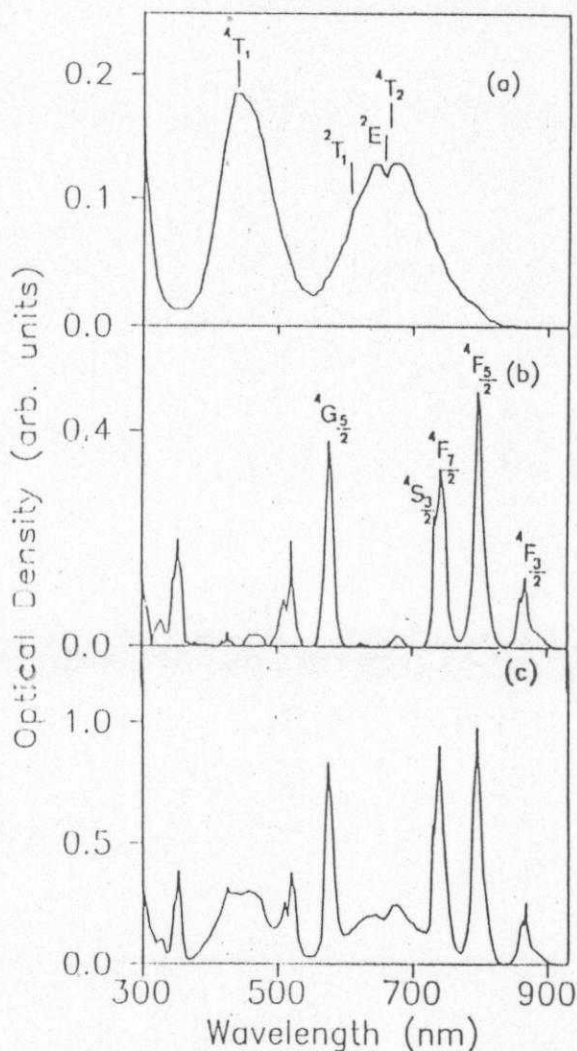
Fig.18 Room-temperature absorption spectra of (a) Cr^{3+} (0.2%) singly-doped BIGaZYTZr fluoride glass, (b) Nd^{3+} (1%) singly-doped BIGaZYTZr fluoride glass, and (c) Cr^{3+} (0.2%):Nd^{3+} (1%) codoped fluoride glass.

A small 0.05% addition of Nd^{3+} (of 2-3 times larger lifetimes 100-500 µs than for Cr^{3+}) in this glass stabilizes the strong fluorescence from $^4T_2$ state of Cr^{3+} adequate to use as a tunable laser. Nd^{3+} ($4f^3$) exhibits characteristically sharper (reflects large lifetime) $4f - 4f$ transitions in the near IR and visible regions, as demonstrated by the spectra of a purely Nd^{3+} (1%) doped fluoride glass in Fig.18b and a codoped fluoride glass with 0.2% Cr^{3+} (1% Nd^{3+}) in Fig.18c. These lines are useful to induce efficient lasers at selected wavelengths.

III. VIBRATIONAL SPECTROSCOPY

Polyatomic molecules exhibit vibrational as well as rotational spectrum in addition to the electronic spectrum. Each electronic state accompanies 3N-6 (or 3N-5 for linear molecules) fundamental modes of vibration of a molecule of N atoms. In addition, the combination and overtones of these fundamental vibrations also occur sometimes but they usually present very low intensities. Resonance of frequency (energy) as well as symmetry of a combination or overtone with those of a fundamental vibration, or electron-phonon coupling, or Jahn-Teller interactions quite often influence their expected intensity distribution.

Each vibrational state in a given electronic state contains a certain number of rotational levels according to the J values. These are rather closed spaced and can be resolved only at reasonably high resolutions. Obviously, their analysis very precisely predicts the electronic structure, isotope shifts, and site symmetry as well as point group symmetry of the molecule (or the crystal unit cell) in the question. However, there are several other constraints because of which it is not in usual practice. It is mostly limited to basic research only.

Vibrational (IR or Raman) spectra of polyatomic molecules usually lie in the range 10-4000 cm^{-1}. The low frequency range 10-600 cm^{-1} is called far infrared region and that between 200 and 4000 cm^{-1} the mid infrared region. Organic molecules containing closed rings or > CHO, >C=O, $-OCH_3$, $-CH_3$, >NH, $-NH_2$, or -OH chromophores

strongly absorb over 300-4000 cm⁻¹ through the characteristic group frequencies. Inorganic molecules with no such functional groups absorb over lower frequencies 100-800 cm⁻¹. Borate, silicate or phosphate glasses, which form network structure, strongly absorb over 800-1500 cm⁻¹.

## (i)   IR and Raman spectroscopy of 1-formyl -3-thiosemicarbazide

Figures 19 and 20 show infrared and Raman spectra of a typical organic system of 1-formyl -3-thiosemicarbazide (FTSC) in the range 300-4000 cm⁻¹. Its molecular structure is shown in Fig.21. This particular compound is famous for exhibiting tuberculostatic, fungistatic and antibacterial effects[20]. The C-H group vibrations are unambiguously distinguished by studying deuterated compound under the same conditions.

Fig.19
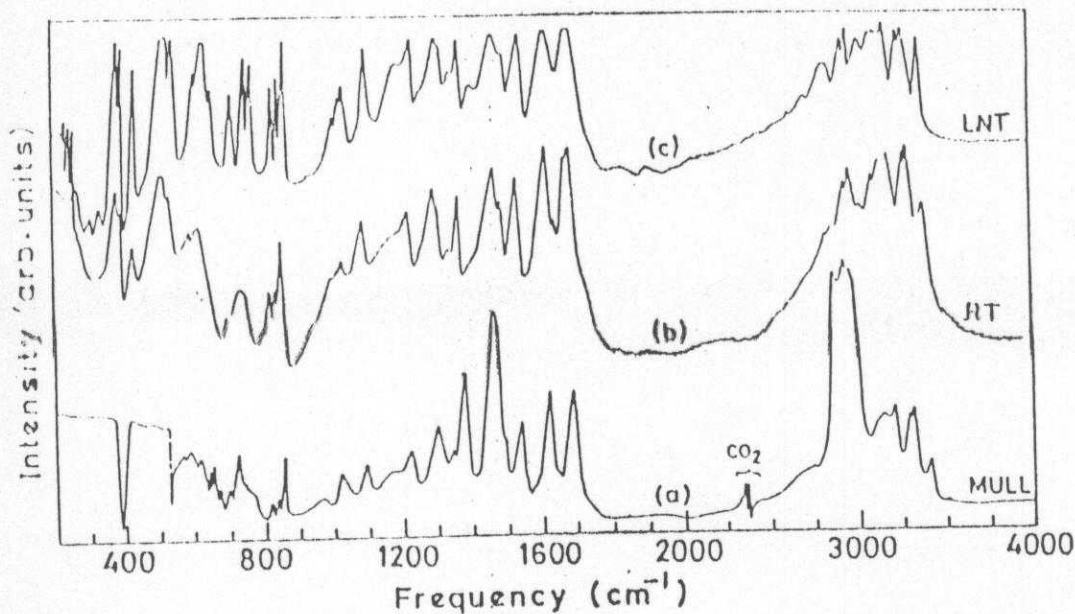
IR of FTSC-d_0 in (a) nujol mull and (b, c) KBr pellet. RT, Room temperature (300 K) Liquid N_2 temperature (77 K).

Fig.20
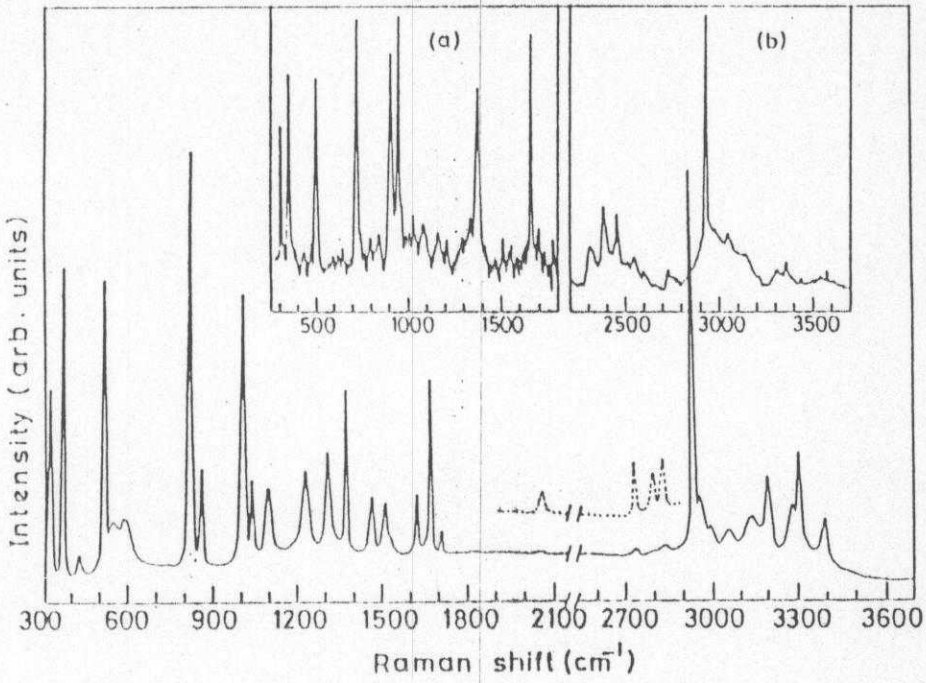
Raman spectrum of FTSC-d_0 at (295 K). In inset are shown Raman spectra of FTSC-d_4 recorded at different intensity scales (say x), with $x = 1$ in region (a) and $x = 5$ in (b).
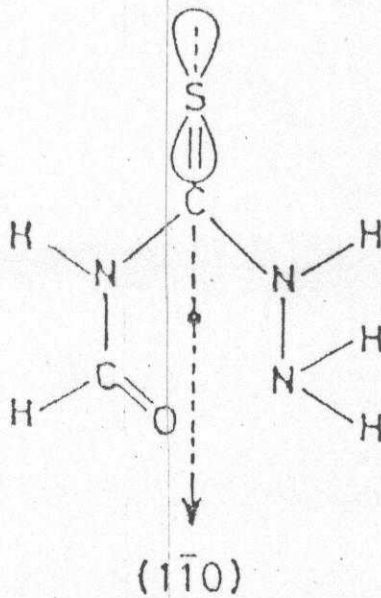

(1$\bar{1}$0)

Fig.21 Molecular Structure of FTSC

FTSC-d_o, in principle, exists in four planar conformers shown in Fig.22. The present vibrational analysis confirmed the (aa) and (ba)
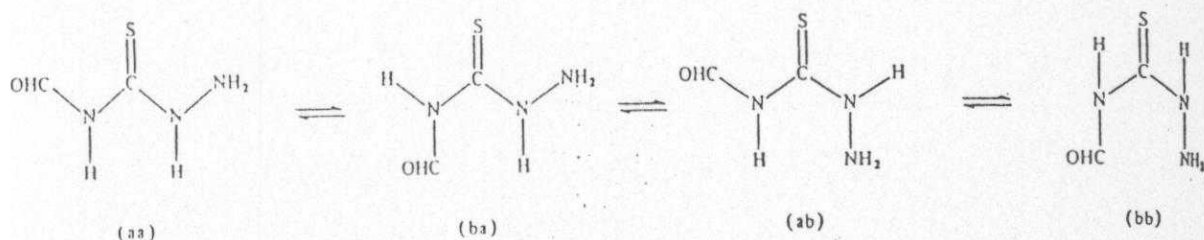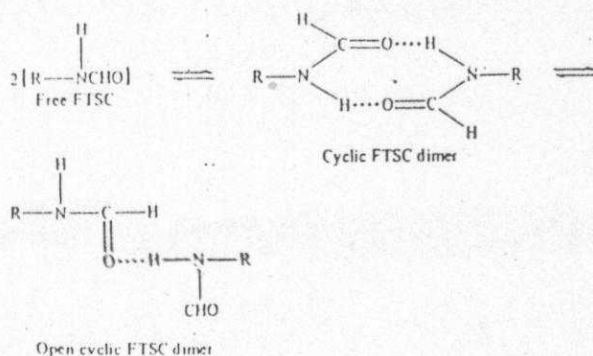

Fig.22 Planar configurational isomers of FTSC-d_0

conformers to be the most stable ones. Those are peculiarly stabilized by intermolecular H-bonded dimer.

where R $\rightarrow$ "-$\overset{\overset{S}{\parallel}}{C}$ - NH - NH$_2$" part of FTSC. Other details about the cyclic or open dimers can be found in Refs. [20-22].

To speculate on the dimer structure we make use of the -C=Ö group vibration. The ν(C=O) bands observed with considerable intensities at ~ 1650 cm^{-1} in the Raman spectrum (g-species characters) do not show their IR counterparts and vice-versa (u-species

characters). This suggests a prominent abundance for the cyclic FTSC dimer (a pseudo D_{2h} molecular symmetry). The prominent Raman band at 1666 cm^{-1} (a band of lowest frequency among the four $v(C=O)$ bands) then can be assigned to the $v(C=O)$ vibration in the cyclic dimer. A large Raman intensity (75 units) as observed for this band is expected for C=O bond oscillation in the above model structure. The cyclic dimer is not so pronounced in the deuterated FTSC-d$_4$, showing a single and weak Raman band at 1658 cm^{-1}. The bands for open-cyclic dimer (a reasonably weak H-bonded system) would fall
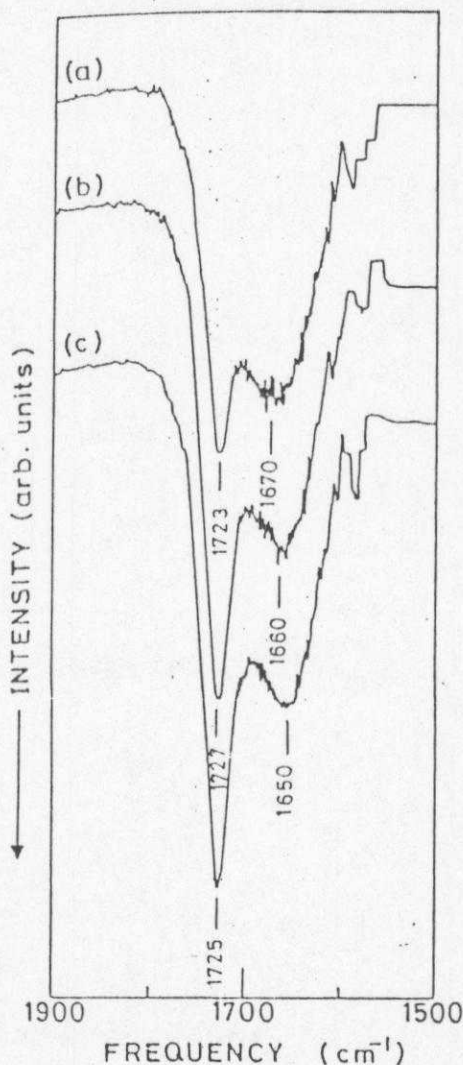

Fig. 23 Typical i.r. spectra (1500–1900 cm^{-1}) of FTSC in ethanol solution. The solution in (b) and (c) is diluted by ~2 and 10 times, respectively, of that of a highly concentrated solution in (a). Intensity is normalized to unity in each case.

at higher frequencies than for the cyclic dimer. These appear to be stabilized in the nujol samples [only one $v(C=O)$ band at 1685 cm^{-1} and two $v(NH_{II})$ bands at 3100 and 3138 cm^{-1} are noticed].

Figure 23 shows IR spectrum of FTSC studied in ethanol solution. The system basically exists in monomer $\rightleftharpoons$ dimer equilibrium showing two $v(C=O)$ bands at 1725 and 1650-1670 cm^{-1}, respectively. The half-bandwidth and peak intensity successively decreases for the dimer band as the concentration of the solution decreases. In view of the symmetry consideration, a sharper (and weak) band is expected to arise in the cyclic dimer (comprising an inherently higher symmetry) structure. It is likely that both the open and cyclic FTSC dimer structures exist in the solution, and the latter structure essentially stabilizes on the lower concentrations.

(ii) Raman spectroscopy of metal$\rightarrow$ semiconductor transition in BaPb$_{1-x}$Bi$_x$O$_3$

BaPb$_{1-x}$Bi$_x$O$_3$ displays a very interesting phenomenon. It undergoes metal to semiconductor transition at x~ 0.35. Here, Raman spectroscopy is very helpful to understand the structural transformation taking place as a function of x.

Figure 24 summarizes Raman spectra of BaPb$_{1-x}$Bi$_x$O$_3$ single crystals at low temperatures 26-31K. The crystal structure is orthorhombic for x < 0.95 and monoclinic for x > 0.95. The variation of intensities of the characteristic peaks against x is given in Fig.25.

The peaks in the range 500-600 cm^{-1} are assigned to ring breathing mode of Pb(Bi)O$_{6/2}$ octahedron as proposed by Sugai[23]. In the semiconducting region x > 0.4, two peaks are observed. The intensity in the higher-frequency peak at ~ 600 cm^{-1} regularly decreases with

increasing x between 0.4 and 1.0, while regularly increases in the lower frequency peak at ~ 560 cm^{-1}. Peculiarly enhanced intensity in 560 cm^{-1} band occurs due to resonance Raman effect with the optical bandgap at 2.15 eV. Fig.26 shows Raman spectrum of $BaBiO_3$ at 39K measured with λ_{exc} = 514.5 nm (2.14 eV) Ar^+ laser line. As expected, resonant peaks for multiple transitions of 566 cm^{-1} phonon are observed upto the fifth order.
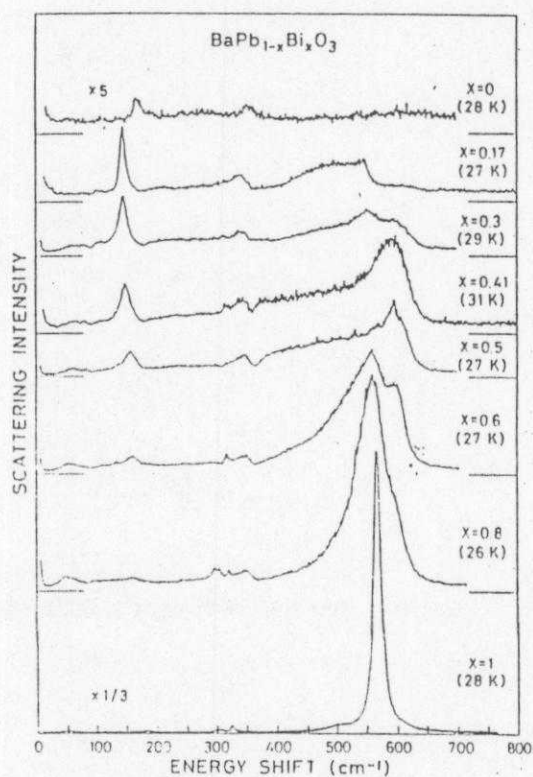

Fig.24 Raman spectra from $BaPb_{1-x}Bi_xO_3$ at low temperatures.
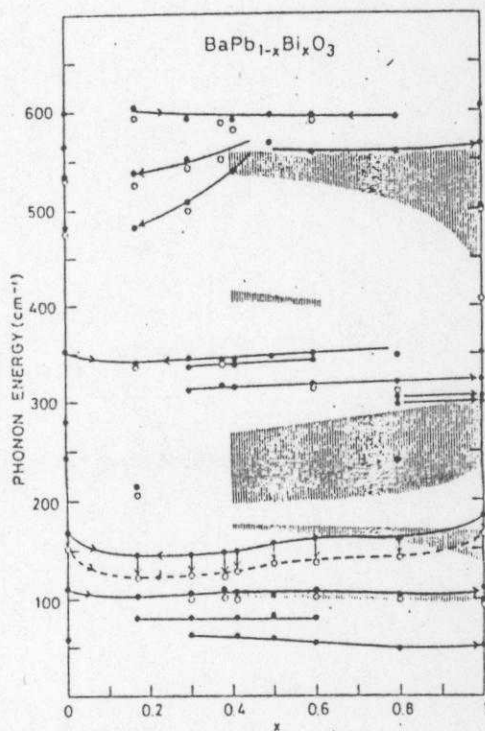

Fig.25 Phonon energies in $BaPb_{1-x}Bi_xO_3$ as a function of x. The filled circles indicate the energies of Raman active modes at about 27 K and the open circles at 273 K. The thick arrows show the direction of increasing scattering intensity. The upper edges of the shaded areas show the LO phonon energies and the lower edges the TO phonon energies.
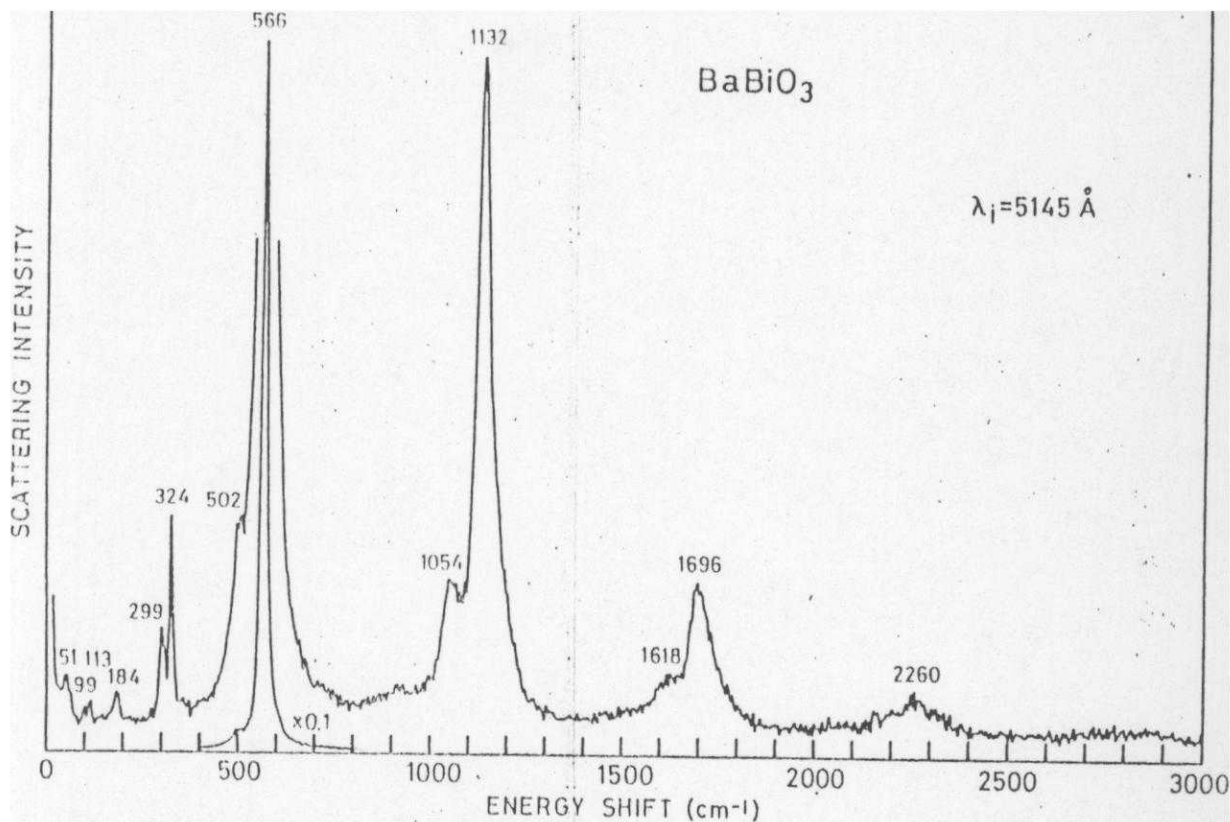
Fig.26 Resonant Raman spectra in BaBiO₃ at 39 K.

(iii) IR and Raman spectroscopy of glasses

IR or Raman spectroscopy successfully applies to inorganic or organic glasses (including the polymers), which do not have any ordered structures. For example, Fig.27 shows a typical IR absorption spectrum of amorphous SiO_2 film begween 900 and 1400 cm⁻¹. Two well resolved bandgroups at 1080 and 1240 cm⁻¹, assigned to TO and LO modes of SiO_2 network, have been observed.
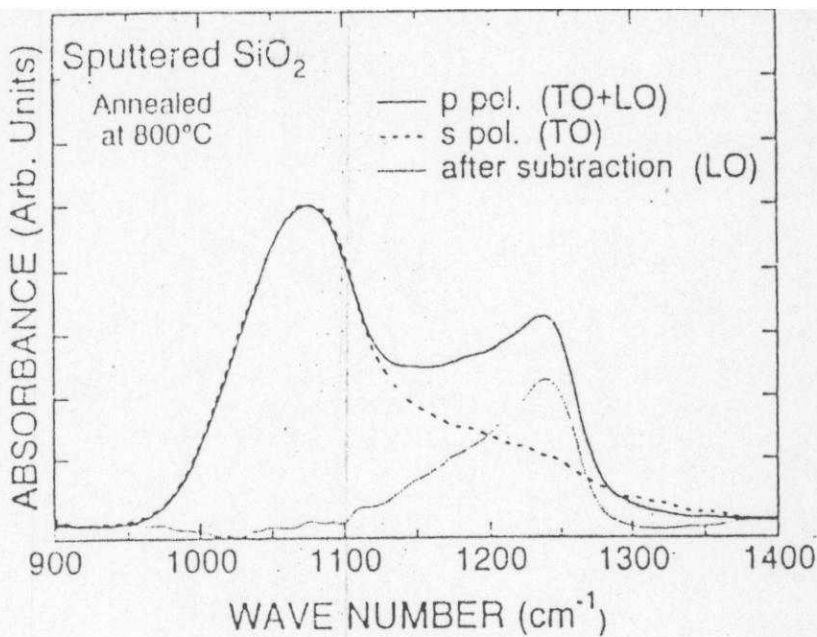
Fig.27 IR-absorption spectra of a pure SiO$_2$-sputtered film measured under 45° oblique incidence. Solid and broken lines represent the spectra obtained with p- and s-polarized incident light, respectively. The dotted line is obtained by subtracting the spectrum for the s polarization from that for the p polarization.

Figure 28 describes influence of a small addition of Ag$_2$O or P$_2$O$_5$ additives in a 40BaO-25Fe$_2$O$_3$-35B$_2$O$_3$ glass. These additives help formation of a purely amorphous structure of the present composition by reducing number of nonbridging oxygens (Fig.29) on boroxol rings in the associated network. As a result, the frequencies of all characteristic B-O stretching modes are enhanced by 3-4% while the corresponding B-O bending frequency at ~ 740 cm^{-1} (in Fig.30) is consistently lowered by the same factor.
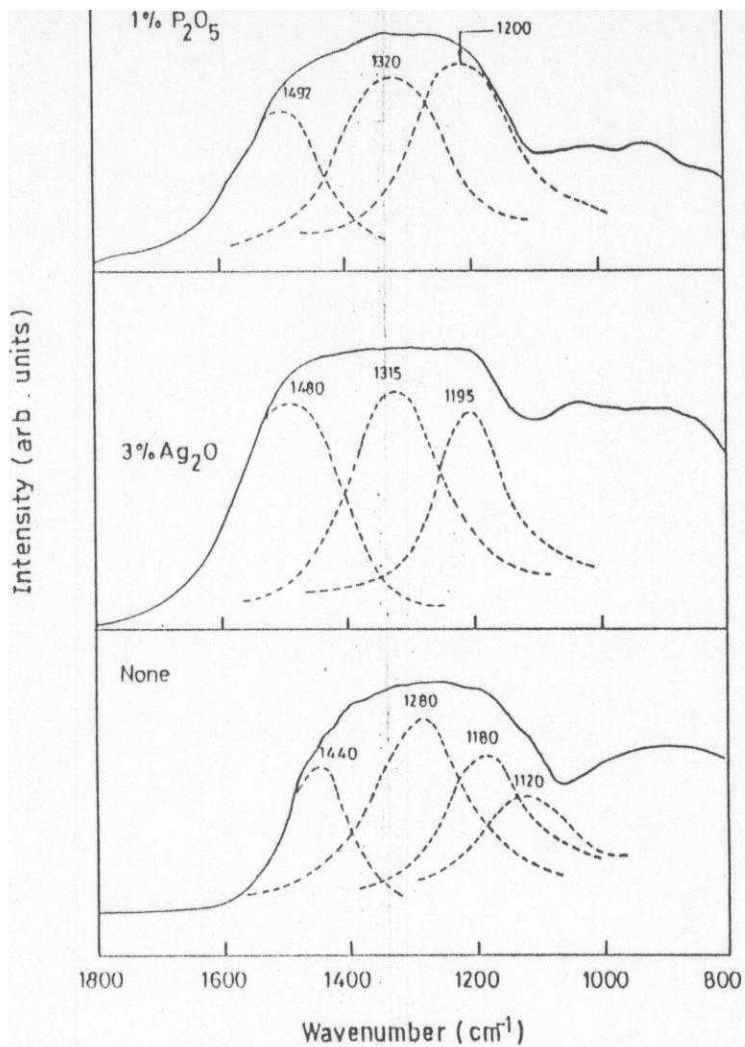
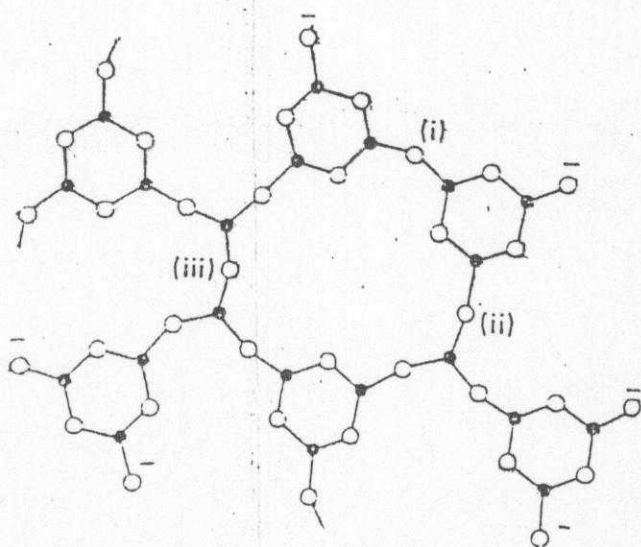Fig.28 IR spectra of borate glass in 800-1800 cm⁻¹ region.
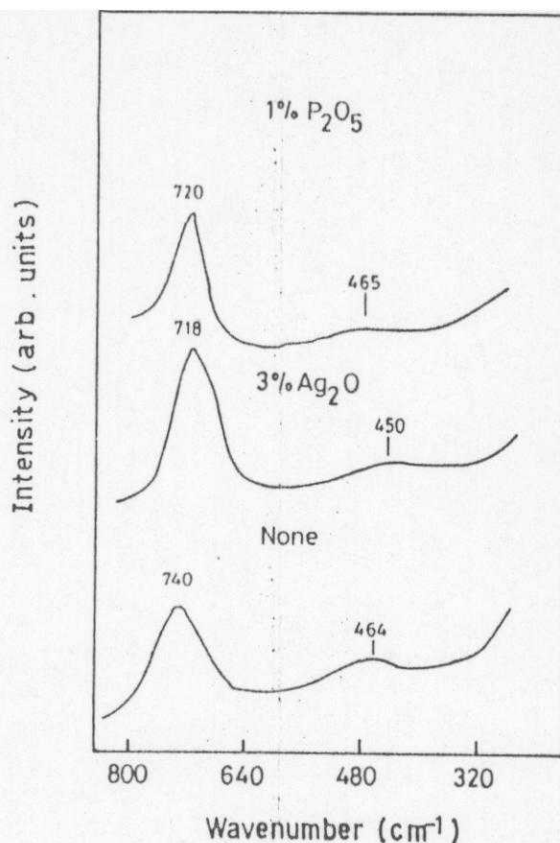

Fig.29 Network structure of borate glass.

Fig.30 IR spectra of Fig.28 in 320-800 cm^{-1} region.

Obviously, the IR or Raman spectroscopy of these glasses is very rewarding in unambiguously determining their structures, and hence provides accurate analysis of their traces in minerals or other materials, not possible to trace out by X-ray diffractometry or other techniques. It applied together with differential scanning colorimetry provides the kinetics and the kinetic parameters of impurity induced structural transformation or thermal induced recrystallization of these structureless materials. It is also useful to study the oxides inclusions (which usually occur in finely dispersed amorphous or nanocrystalline material) in metals and alloys.

REFERENCES :

1. S.Ram., K.Ram and B.S.Shukla, *J. Mat.Science* **27**, 522 (1992)

2. D.K. Sardar, M.D.Shina and W.A Sibley, *Phs. Rev.* B **26**,2382. (1982)

3. S.Ram and K.Ram, *J. Mat. Science* **23**, 4541 (1988).

4. M./Wolfsberg and L. Helmhol2, *J. Chem. Phys.* **20**, 837 (1952).

5. K.Today and S.Morita, *Appl. Phys.A.* **33**, 231 (1984).

6. S.Morita and K.Toda, *J. Appl. Phys.* **55**, 2733 (1984).

7. K.Tota and S.Morita, *ibid*, **57**, 5325 (1985).

8. C.Testelin, C.Rigaux, A.Mauger, A.Mycielski and C.Julien, *Phys. Rev.* B. **46**, 2183 (1992)

9. R.Heitz, A.Hoffmann and I.Broser, *Phys. Rev.* B. **45**, 8977 (1992).

10. H.A.Weakliem, *J. Chem. Phy.* **36**, 2117 (1962).

11. H.Maier and U.Scherz, *Phys. Rev.* A, **140**, 2135 (1965).

12. A Hoffmann, I.Broser, P.Thwian and R.Heitzz, *J. Cryst. Growth* **101**, 532, (1990).

13. J.Bajaj, S.H.Shir, P.R.Wewman, J.E.Huffmann and M.G.Stapelbrook, *J. Vac. Sci. Technol.* **A4**, 2051, (1986).

14. P.M.Volz, C.H.Su, S.L.Lehoczky and F.R. Szofran, *Phy. Rev.* B **46**, 76 (1992).

15. N.Nagelatos, D.Wehe and J.S.King, *J. Chem. Phys.* **60**, 3613 (1974).

16. L.N.Feuerhelm, S.W.Sibley and W.A.Sibley, *J. Solid state Chem.* **54**, 164 (1984).

17. K.A.Gschneidner and L.Eyring "*Hand Book of Physics and Chemistry of rare earths*", Elsevier., Amsterdam/New York (1979).

18. S.Ram and S.K.Sinha, *J. Lumin,* **66,** 225 (1987).

19. S.Ram, *J. Raman Spectros.* **18,** 537 (1987).

20. S.K. Sinha, S.Ram and O.P. Lamba, *Spectrochim Acta* **44A,** 713 (1988).

21. S.Ram, Can, *J. Chem.* **62,** 1845 (1984).

22. S.Ram, K.Ram and J.S.Yadav, *J. de Chem. Phys.* **81,** 77 (1984)

23. S.Sugai, *Phy. Rev. B* **35,** 3621 (1987).